Understanding Molecular Aggregation of Ligand-protected Atomically-Precise Metal Nanoclusters

Vikas Tiwari and Tarak Karmakar*

Department of Chemistry, Indian Institute of Technology, Delhi, Hauz Khas, New Delhi 110016, India

E-mail: tkarmakar@chemistry.iitd.ac.in

Abstract

Atomically precise ligand-protected nanoclusters (MPC) have emerged as an important class of molecules due to their unique structural features and diverse potential applications, including nano-electronics, bio-imaging, as sensors and drug carriers. Understanding the atomistic details of their intermolecular interaction is of paramount interest for designing, synthesizing, and system-specific applications. Crystal structures of various MPCs provide details related to molecular packing and intermolecular interactions. While these experiments reveal macroscopic, mostly static properties, they are often limited by the spatial and temporal resolutions in delineating the microscopic dynamical details. Here we apply molecular dynamics and enhanced sampling simulations to study the aggregation of $Au_{25}(p\text{MBA})_{18}$ MPCs in the solution phase. The MPCs interact *via* both hydrogen bonds and π-stacks between the aromatic ligands to form stable dimers, oligomers, and periodic crystals. The free energy profiles obtained from enhanced sampling simulations of dimerization reveal a pivotal role of the protonated states of the ligands as well as the solvation shell in mediating the molecular aggregation process in solution. In the solid phase, the MPCs' ligands have suppressed conformational flexibility owing to many facile intermolecular hydrogen bonds and π-stacks. Our work provides unprecedented molecular-level details of the aggregation process and conformational dynamics of MPCs ligands in the solution and crystalline phases, which will help rational design of new MPCs with specific properties.

INTRODUCTION

Monolayer-protected metal nanoclusters (MPCs) consist of a metal core confined in a small volume that is protected by several organic ligands.[1,2] In recent years, MPCs have gained huge attention due to their high atomic precision and the direct relationship of their physical and chemical properties with their unique geometries.[3,4] Atomically precise structures of MPCs have led to numerous potential applications in the field of catalysis, biosensors, chemical imaging, and energy conversion.[5–12] Among the stable MPCs, $Au_{25}(SR)_{18}$ is the most extensively studied MPC both experimentally and theoretically. Due to the high stability, small size, and easy preparation methods $Au_{25}(SR)_{18}$ is referred to as the *brightest molecular star* in the nanocluster field.[13] Ever since its synthesis and characterization, its physicochemical properties like catalysis, optical and magnetism have been explored in great detail.[14–19] Most of the $Au_{25}(SR)_{18}$ nanoclusters studied till date contain water-insoluble ligands, whereas some water-soluble thiol-based ligands such as p-mercaptobenzoic acid[20] (pMBA), 11-mercaptoundecanoic acid[21] (11-MUA), cysteine[22] (Cys), captopril[23,24] (Capt), and glutathione[25,26] (GSH) have also been used to synthesize MPCs. Due to the presence of these ligands, the nanoclusters become water soluble, which has high biocompatibility, good photostability, and low toxicity, hence, their use in cell labeling, phototherapy, and biosensing is highly promising.[27] Compared to conventional fluorescent materials water-dispersible nanoclusters show higher photostability and strong photoluminescence, hence, they are also excellent candidates for fluorescent image probing.[28,29] Water soluble MPCs can also be considered as potential candidates for carrying out catalysis in the aqueous medium.[27] Some recent reports have shown biological applications of water-dispersible MPCs including anticancer activity,[30] anti-Alzheimer's drug,[31] and as a delivery vehicle for an anticancer drug.[32,33]

Recently some insights into the aggregation of MPCs and their interaction with the biological environment have been provided using experimental as well as computational methods at atomistic and coarse-grained levels.[34–42] Vanzan *et al.,* studied the dimerization of three different Au_{25}-based nanoclusters functionalized with hydrophobic ligands in dichloromethane

solvent using metadynamics (MetaD)simulations.[38] In another work, Shen *et al.*, studied the aggregation of a gold cluster containing Au_{314} core at different pH using a coarse-grained (CG) model.[37] These studies provided valuable insights into the structural and functional details of MPCs in multiscale resolution. However, a more detailed atomistic description of the aggregation of MPCs and the dynamics of their ligands in the solution and solid phases require further investigation. Furthermore, the role of solvent in modulating both the aggregation and dissolution processes requires special attention.

In this work, we have focused on studying the molecular aggregation of highly water-soluble MPCs, $Au_{25}(p\text{MBA})_{18}$ using atomistic molecular dynamics (MD) and enhanced sampling (ES) simulations. In particular, at first, we studied the dimerization of two $Au_{25}(p\text{MBA})_{18}$ monomers in aqueous as well as methanol solutions. This was followed by the study of the self-assembly of MPCs in both solvents. To understand the solubility of MPC crystals, we have carried out long MD simulations of a small crystal immersed in water and methanol solutions, respectively. Finally, a periodic crystal of $Au_{25}(p\text{MBA})_{18}$ has been investigated to understand the lattice stability, molecular packing, and ligand dynamics in the crystalline phase. The atomistic insights into the self-assembly process and the aggregated structures from our study may help design MPCs with specific properties in a heuristic approach.

RESULTS & DISCUSSION

Dimerization

The first step in the aggregation process is the formation of a dimer, and studying the dimerization process can reveal valuable information related to the MPCs self-assembly mechanism. Generally, the MPCs with pMBA ligands exist in various charged states - from fully protonated to deprotonated states depending upon the pH of the solution. In a study by Koivisto *et al.*,[43] it has been found that the pK_a of pMBA ligands in the $Au_{102}(\text{pMBA})_{44}$

nanoclusters (pK_a = 6.20) is ∼2 units higher than the free pMBA (pK_a = 4.13). So we expect that some of the MPC ligands' carboxylate groups will be deprotonated. Here we followed a systematic approach and modelled MPCs with varying degrees of deprotonation (MPC_{0d} - 0% MPC_{25d} - 25%, MPC_{50d} - 50%, MPC_{75d} - 75% and MPC_{100d} - 100%) of the ligands. These systems approximately mimic different pH states of the system.[37]

Two $Au_{25}(p\text{MBA})_{18}$ (MPCs) molecules were placed approximately at a center of mass (COM) distance of 5 nm in a cubic box and simulated in explicit water. After ∼20 ns of simulation time, a dimer was formed with the COM-COM distance of ∼1.3-1.4 nm. The dimer remained intact for the rest of the simulation (500 ns). For comparison, another independent simulation was also performed in methanol (discussed in SI section S1.1). The reorganization of MPCs ligands is one of the crucial factors responsible for the aggregation process. From the literature, it is known that MPC ligands in their monomeric state form intra-cluster π-stacks and organize themselves in a group of 2-3 ligands.[44] During the formation of dimers, trimers, or multimers, the MPCs ligands reorient themselves to facilitate the aggregation process. To understand ligand dynamics at the molecular level, we focused on one MPC of the dimer and carried out angle distribution analysis based on the configurations collected from 100 ns unbiased simulation trajectory. The angle (θ) between molecular vectors of different ligands of MPC was chosen for the analysis (Fig 1b). After careful observation, we selected a few representative ligands L1-L7, (highlighted in green color in Fig 1a) that showed the significant deviation in the angle during the transition from monomeric to the dimeric state. Figure 1c shows the evolution of four selected angles between L1-L2, L2-L4, L5-L6, and L1-L7. The dimerization accompanies both positive and negative deviations in these angles. Interestingly, ligands reorganization was found to take place after the initial encounter of the monomers forming a loosely bound dimer, the dimerization began at ∼20 ns but the ligand reorganization took place after ∼35 ns of simulation. During the reorganization event, the ligands that are present near the dimer interface, direct outwards (carboxylic acid head group) to increase the hydrophobic contact between the MPC ligands

via π-stack formation. This phenomenon has been named as the '*snorkeling effect*' (Fig 1a) in the context of ligand-coated nanoparticles self-assembly.[45,46] A movie showing the *snorkeling effect* in our case can be found in ESI section xx. During the reorganization process, the ligands exchange their π-stacking partners with each other as shown in Figure 1a.

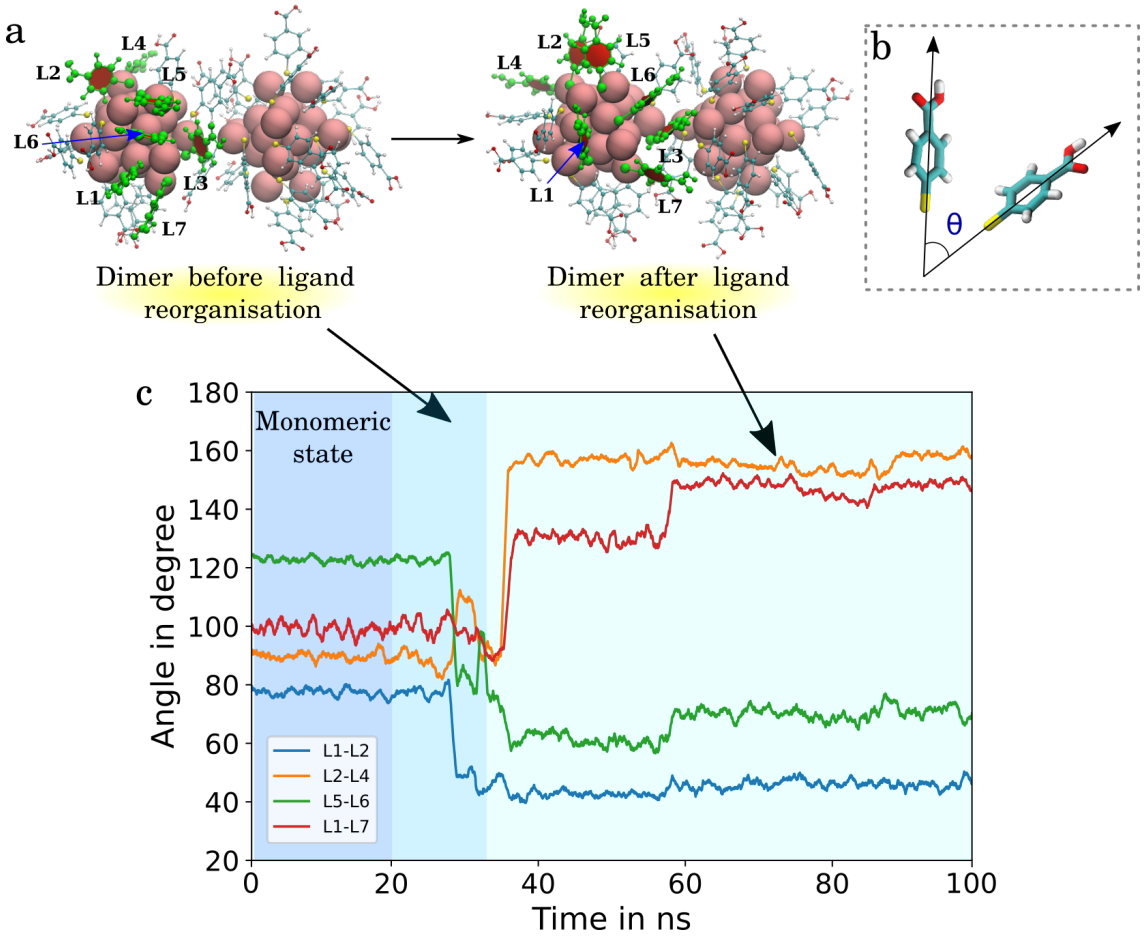

Figure 1: Ligand-ligand angle analysis of unbiased 100 ns trajectory of dimerization. a) Ligand orientation reordering during dimerization showing "*snorkeling effect*", b) Depiction of angle taken into account for this analysis, and c) Plot of selected angles between various ligands with respect to simulation time.

Equilibrium MD simulations provided limited short-timescale atomistic details of the dimerization process. Hence to efficiently sample the dimerization processes and unveil the energetics for the dimer formation, we carried out on-the-fly probability-based enhanced sampling (OPES) simulations.[47] OPES, a recent evolution of the popular MetaD method, is an enhanced sampling method in which the bias potential (V(s)) is constructed by pe-

riodically depositing repulsive Gaussians that, in turn, modify the equilibrium probability distribution using a reweighing method.[47] The bias potential, V(s) is defined as a function of one or a set of collective variables (CV≈s) that are a function of atomic coordinates. These CVs are chosen in such a way that they can distinguish a system's metastable states, and when biased, help the system transit between these states. A rational choice of a CV for a dimerization process would be the COM distance between the two MPC clusters. Hence, we carried out our first set of OPES$_E$[48] (its explore variant) simulations with a CV, s_1 defined as the distance between the COMs of metal cluster Au atoms (ligands being highly flexible are not the best choices to define COM) of the two MPCs. Although we anticipated s_1 to be a good CV for the dimerization process, the OPES simulation did not sample the dimeric and monomeric states efficiently. Soon we realized that the desolvation of coordinated solvents around the MPC clusters can also accompany the dimerization of MPCs, and we introduced a second CV, s_2 which is defined as the number of coordinated solvent molecules around an MPC.

Using these s_1 and s_2 CVs, an OPES$_E$ simulation of MPCs (fully protonated) dimerization in water was performed for 2 μs. The plot s_1 *vs* simulation time (t) shows many back-and-forth transitions between the monomeric and dimeric states (Fig. 2a) indicating an efficient exploration of the two metastable states. In the simulation trajectory, we observe the formation of various dimeric states among which three dimeric states shown in Fig. 2b-d were found to be quite stable. These dimeric states differ on the basis of inter-cluster distances, number of H-bonds, number of π-stacks, and the pattern of H-bonds and π-stacking interactions. Dimer_1 shows a special zipping pattern of π-stacks connecting two MPCs from three inter-cluster π-stacks, each further extending *via* intra-cluster π-stacking (Fig. 2b). Dimer_1 shows the lowest COM-COM distance of ∼1.3 nm whereas, more frequently observed Dimer_2 (Fig. 2d) has a distance of ∼1.5 nm. Dimer_2 is characterized by two extended inter-cluster π-stacking series along with two inter-cluster H-bonds. An interesting symmetrical interaction pattern of multiple π-stacks and H-bonds between the MPCs

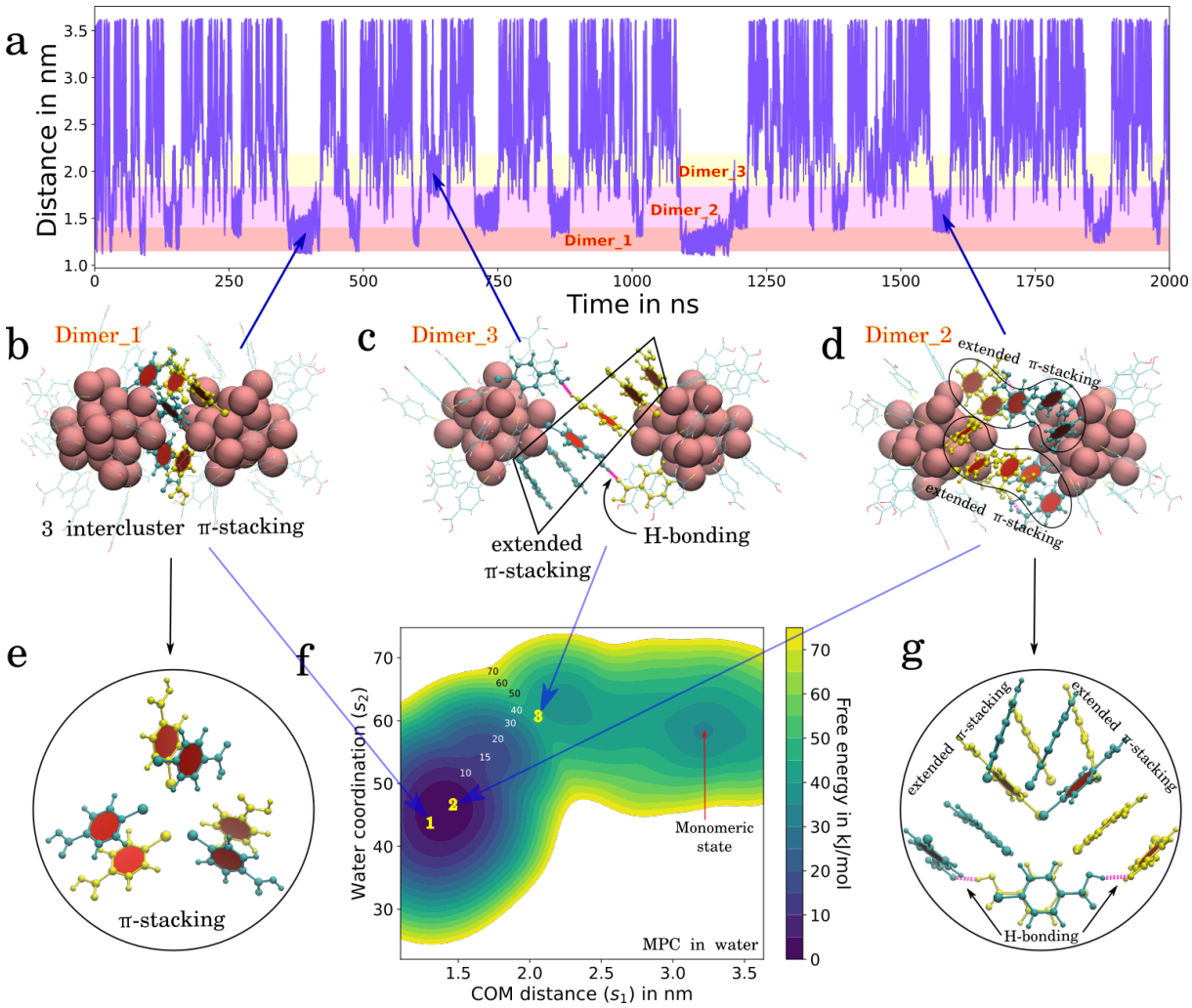

Figure 2: (a) s_1 vs OPES$_E$ simulation time plot showing transitions between various dimeric and monomeric states, (b) Dimer_1 with average COM distance of 1.35 nm showing three inter-cluster π-stacking, (c) Dimer_3 with average COM distance of 2.0 nm showing extended inter-cluster π-stacking with two cross H-bonds, (d) Dimer_2 with average COM distance of 1.50 nm showing two extended inter-cluster π-stacking with two cross H-bonds, e) inter-cluster π-stacking in (b) showing only inter-facial ligands, (f) Free energy surface as a function of s_1 vs s_2, (g) inter-cluster π-stacking and H-bonds in (d) showing only inter-facial ligands forming a symmetrical shape. Color code: cyan: MPC1 ligands and yellow: MPC2 ligands.

ligands has been observed in this dimer (Fig. 2g). Another intermediate Dimer_3, relatively short-lived dimer, has been identified at a COM-COM distance of ∼2 nm showing only one extended inter-cluster π-stack and two H-bonds.

The free energy profile was obtained by reweighting the deposited bias, and the free

energy of dimerization for the fully protonated MPCs is ∼40-50 kJ/mol (Fig. 2f).

So far we have discussed the case of fully protonated MPCs (MPC_{0d}). Now, we switch our attention to the systems with varying deprotonated states. For each of the MPC_{25d}, MPC_{50d}, MPC_{75d}, and MPC_{100d} systems, we carried out 2 μs $OPES_E$ simulation. The free energy as a function of the distance CV (s_1) is calculated by reweighting the deposited bias. The free energy profiles for all four systems are shown in Figure 3a. We observe a systematic evolution of the free energy profiles as a function of the degree of deprotonation of the MPC ligands. The dimer basin is much deeper (∼60-70 kJ/mol) in the case of MPC_{25d} and MPC_{50d} compared to the fully protonated MPC_{0d} and deprotonated MPC_{100d} systems. In MPC_{0d}, protonated ligands form multiple numbers of H-bonds, however, the propensity of the H-bonds formation is more in the case of MPC_{25d} and MPC_{50d} systems due to the presence of a few -COO^- groups that can form strong H-bonds. With further increase in deprotonated ligands (>80%), the MPCs repel each other making the dimer less stable. This also correlates with the fact that more carboxylate anions exposed to water can get stabilized by solvent coordination making fully deprotonated MPCs more soluble in water. Our observation corroborates well with the experimental finding in ref. 43 which showed increased solubility of $Au_{25}(p\text{MBA})_{18}$ in water with more number of deprotonated pMBA ligands in MPCs.

Aggregation and dissolution

Self-assembly: To further understand the aggregation of $Au_{25}(p\text{MBA})_{18}$ MPCs in the solution phase, we carried out equilibrium MD simulations of ten randomly dispersed monomers of a partly deprotonated (MPC_{25d}) MPCs in water. For comparison, we additionally performed a similar simulation in the methanol solvent. In both solvents, we observe the formation of self-assembled clusters, but the nature and size of these clusters are different in water and methanol. In the case of water, a big stable cluster was formed within ∼50 ns of simulation time, while in the case of methanol, initially a few small clusters were formed,

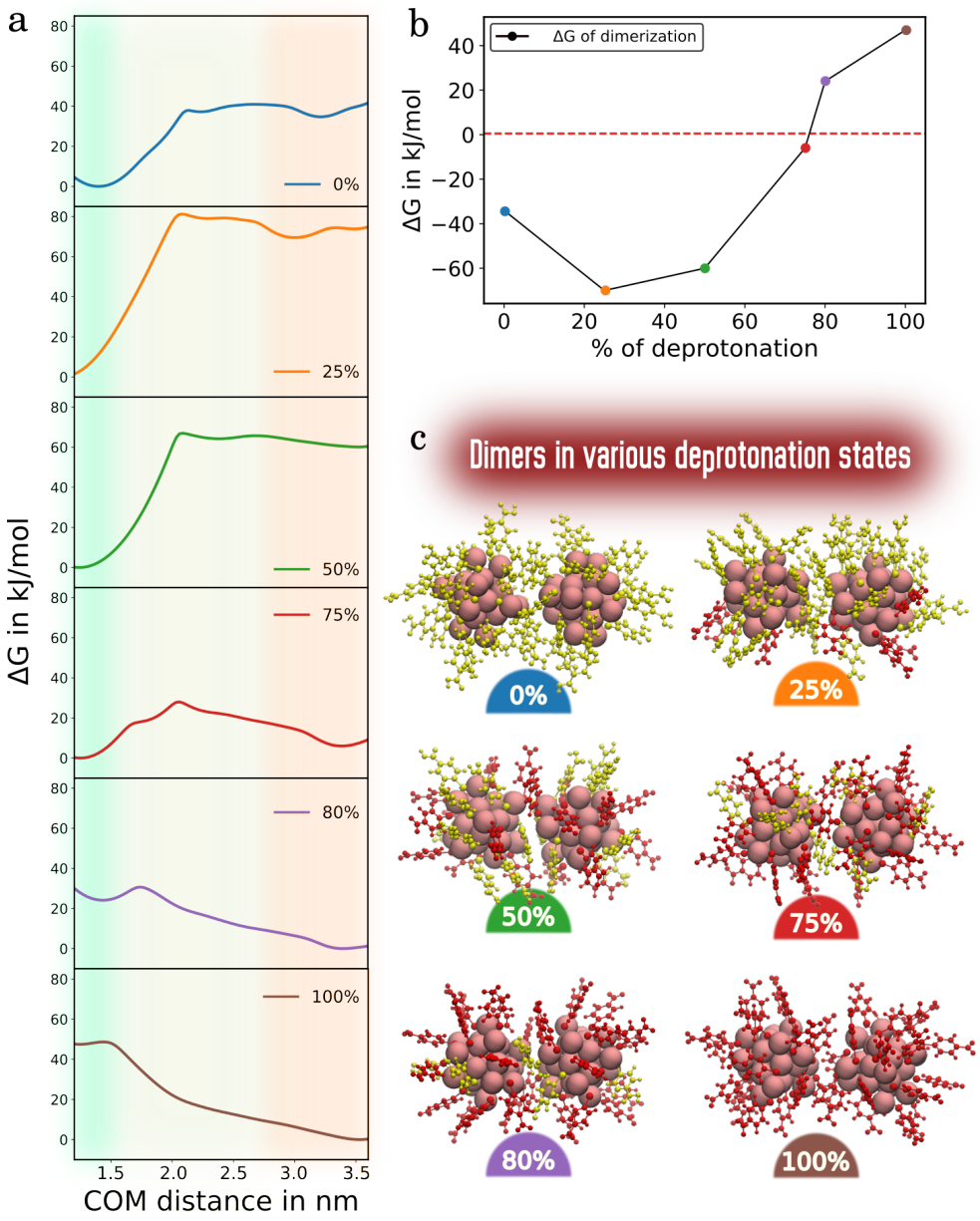

Figure 3: (a) Free energy profile as a function of COM-COM distance CV (s_1) of MPCs for various deprotonated states, (b) plot showing the variation of free energy of dimerization with respect to the fraction of deprotonation, c) dimeric states of MPC with varying degree of deprotonation.

that the later stage, beyond ∼400 ns, coalesce to form a large cluster. This outcome is not surprising, and it is related to the higher solubility of MPCs in methanol than in water,[43] which is further discussed in the subsequent section.

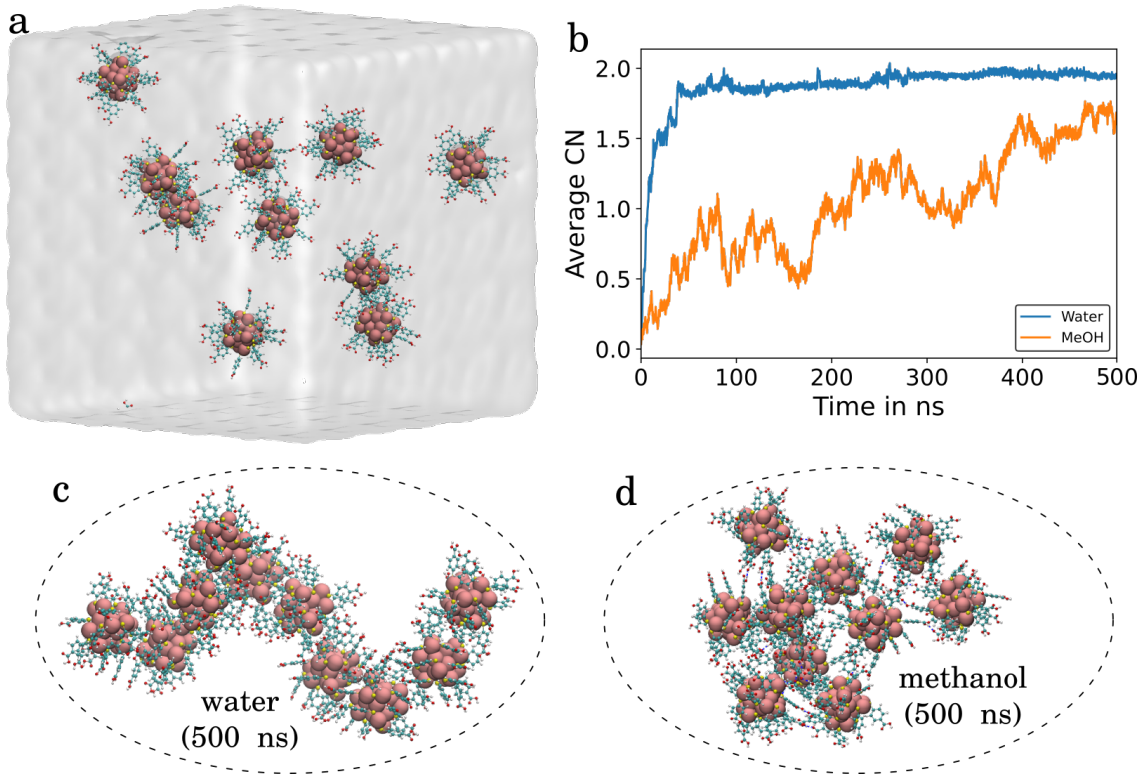

Figure 4: a) Initial setup for studying the self-assembly of MPC_{25d} - 10 monomers dispersed randomly in water/methanol, b) Evolution of average coordination number of MPCs through 500 ns of simulation time, c) final form of the cluster formed in water after 500 ns of the simulation, d) final form of the cluster formed in methanol after 500 ns of the simulation.

Dissolution: MPCs containing pMBA ligands are soluble in water and alcoholic solvents.[43] In particular, MPCs are more soluble in methanol than water, and the solubility increases as the fraction of deprotonation increases.[43] For a qualitative analysis of the solubility of the fully protonated MPCs, a small crystal containing 13 MPCs, selected from the face-centered-cubic (FCC) periodic crystal of $Au_{25}(p\text{MBA})_{18}$, was placed in both water as well as methanol, and the two systems were simulated in an NPT ensemble for 1 μs. Within a few hundreds of nanoseconds, the MPCs started to deviate from their respective lattice positions in the crystal. The overall crystal distortion was more in methanol where two MPC molecules were detached from the cluster in ~200 ns simulation time. Whereas in water, we did not observe any dissolution till 1 μs of simulation time except for slight distortion of the crystal. (Fig. S3) In the previous section, we observe that the dimer basin in the case of

water (Fig. 2) is much deeper than in methanol (SI section S1.2), which also explains that the aggregated state is more stable, and thereby, the crystal dissolution is less favorable in water than in methanol.

Periodic lattice

Recently, Yao *et al.* have synthesized $Au_{25}(p\text{MBA})_{18}$ supercrystals in two polymorphic forms *viz.,* face-centered cubic (FCC) and hexagonal closed packing (HCP).[49] In the presence of an excess of tetraethylammonium cations, the $Au_{25}(p\text{MBA})_{18}$ crystalizes in HCP form instead of the FCC lattice. MD simulations helped them decipher the interactions of the tetraethylammonium cations with the pMBA ligands of the metal clusters.

In our work, we continue enriching our understanding of the ligands dynamics in the FCC crystal. Towards this goal, we simulated an FCC crystal of $Au_{25}(p\text{MBA})_{18}$ and analyzed various non-covalent interactions responsible for the crystal stability. As the single crystal structure for $Au_{25}(p\text{MBA})_{18}$ is not available, we took the inspiration from Yao's work and built a 2×2×2 FCC periodic supercell lattice to study the crystal stability and ligands dynamics in the solid phase. An equilibrium simulation of this periodic crystal in the NPT ensemble was carried out at a temperature of 300 K and pressure of 1 bar for 100 ns. To check the stability of the crystal, its lattice volume is plotted as a function of the simulation time (Fig S4a). The lattice volume converged quickly and fluctuates around the mean value of 121 nm^3. From this mean box volume, the unit cell parameter was calculated to be 2.48 nm. The average COM-COM distance between two MPCs is ∼1.75 nm which is an intermediate value between Dimer_2 and Dimer_3 COM distances discussed previously.

In 2016, Häkkinen's group studied the conformational dynamics of pMBA ligands of $Au_{102}(\text{pMBA})_{44}$ using NMR, DFT, and MD simulations, and observed a diverse set of the orientational ordering of the MPC ligands in the solution phase.[41] Their study was focused on the dynamics of ligands in fully solvated MPCs (dilute solution), which provided details of fluctuations in ligand's orientation. However, in the solid phase, the ligands have restricted

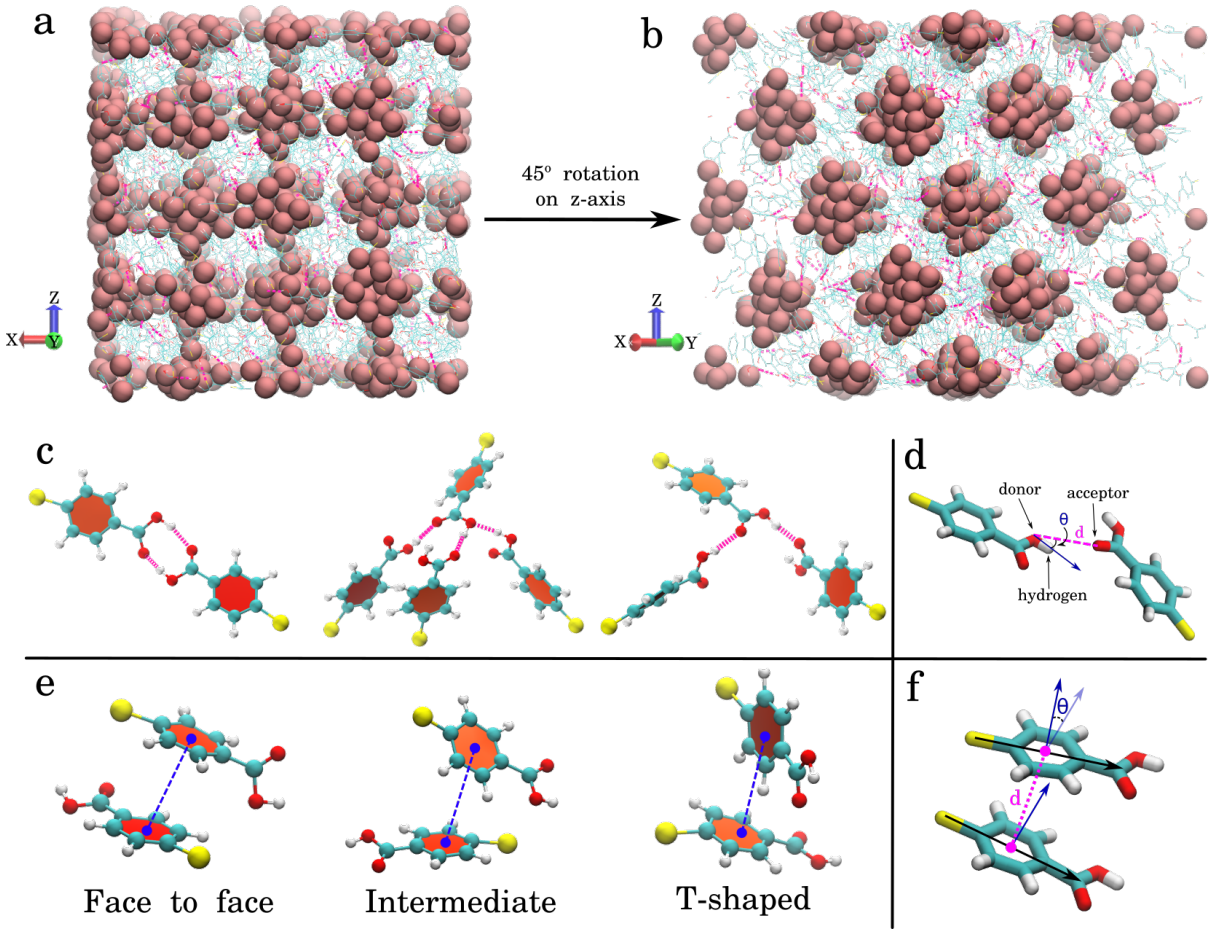

Figure 5: Periodic crystal lattice: a) 2×2×2 FCC supercell after 100 ns of simulation, b) another view of crystal a regular arrangement of MPC clusters in the crystal, c) Various hydrogen bond network and π-stack interactions helping in stabilizing the crystal, d) Graphical representation of vectors, distances, and angles used in the case of H-bonding (black, vector from H-bond donor atom to hydrogen; magenta dashed line, the distance between H-bond donor and acceptor atoms, e) Types of π-stacking observed in the MPC crystal, f) π-π stacking (black, molecule vector; blue, normal to the benzene ring plane of one molecule; magenta dashed line, the distance between molecule centers).

motions and take part in intermolecular interactions with neighbouring MPC ligands. Interestingly, in the periodic lattice, the ligands exhibit directional ordering; in one direction, more ligands participate in the intermolecular interactions, and orthogonal to it, less number of ligands interact (see Fig. S5). To further understand the kind of intermolecular interaction involved in the crystal lattice, we performed H-bond distribution analysis and a systematic π-stack analysis. H-bonds were defined using the cutoff of 0.3 nm for the distance between donor and acceptor atoms and cutoff of 30° for the angle between hydrogen-donor-acceptor

(as shown in the Fig. 5d). The H-bond distribution analysis showed that an average of ∼250 H-bonds per frame were formed, which corresponds to ∼8 H-bonds per $Au_{25}(p\text{MBA})_{18}$ cluster unit (Fig. S4b). The H-bonds formed were of various kinds involving multiple ligands (a few of them are illustrated in Figure 5c). For the π-stack analysis, a cutoff of 0.5 nm for the COM-COM distance between benzene rings of two ligands was used. Angle between the normal vectors of benzene ring plane was used to differentiate between the face-to-face (<30°), intermediate (<50°) and T-shaped (>50°) π-stacks (see Fig. 5f and table 1). Further, the π-stack analysis showed that the propensity of face-to-face π-stacking is more than the T-shaped π-stacks (see Table 1). Along with this, multiple extended π-stacking containing upto five π-stacks were also observed (Fig. S6).

Table 1: Summary of π-stack analysis of a periodic crystal.

Type of π-stacks	**Distance cutoff (nm)**	**Angle cutoff θ in rad (deg)**	**Number of intra-MPC π-stacks**	**Number of inter-MPC π-stacks**
face-to-face	0.5	$< \pi/6$ (30)	102	43
Intermediate	0.5	$< 5\pi/18$ (50)	35	19
T-shaped	0.5	$> 5\pi/18$ (50)	33	16

CONCLUSIONS

In this work, we studied the aggregation of $Au_{25}(p\text{MBA})_{18}$ in water and methanol solvents. We observed that the degree of protonation of the MPCs' ligands largely influences the aggregation propensity. Specifically, the $Au_{25}(p\text{MBA})_{18}$ dimers with 25-75 % protonated ligands show higher stability than the fully protonated or the deprotonated systems. The ligands protonated states, MPCs with mixed charged ligands, and the right selection of solution pH that can control the aggregation behaviour and provide self-assembled states.

Furthermore, the stability of the dimeric state is more in water than in methanol. This can also be correlated with the higher solubility of $Au_{25}(p\text{MBA})_{18}$ crystal in methanol compared to that in water. One can explore the solvent-dependent aggregation behavior to design new MPCs and grow new crystals. We also identified that the intermolecular hydrogen bonds and π-stacks chiefly control the aggregation behavior. Therefore, the properties of the MPCs' ligands, including their capability of forming hydrogen bonds and π-stacks, hydrophobic and electrostatic interactions could also be taken into consideration for future MPCs design. The pertinent atomistic and dynamical insights obtained from our work can guide rational designing of new MPCs with specific properties, and thus, this work contributes towards expanding the scope of this emerging research area.

COMPUTATIONAL METHODS

System setup

The monomer and dimer of $Au_{25}(p\text{MBA})_{18}$ was simulated in a cubic box of volume 7.5 nm^3 filled with water and methanol solvents. A periodic crystal unit cell of MPC was created in FCC crystal system using GROMACS[50] software and a 2×2×2 supercell was generated by replicating the unit cell.

Force field details

Avogadro[51] software was used to create the initial structure of a para-mercaptobenzoic acid (pMBA) ligand, and the NanoModeler server[52,53] was used to create the full MPC structure and topology with varying degrees of deprotonation. It employs the bonded and non-bonded characteristics of the gold-sulfur motifs produced by Pohjolainen *et al.*[54] and Heinz *et al.*[55] (Table SI). Whereas for ligands and methanol, the General AMBER Force Field (GAFF)[56] was used. For water, we have used the TIP3P potential model.

Simulation details

Systems were first minimized using the steepest descent algorithm and thermally equilibrated at temperature 300 K in the canonical (NVT) ensemble. Subsequently, a short NPT simulation of each system was carried out to equilibrate the simulation box. In both NVT and NPT simulations, we have used the stochastic velocity rescaling thermostat. Berendsen barostat was used to equilibrate the sytem's volume and maitain the pressure at 1 bar.[57] In the production NPT simulations, we replaced the Berendsen barostat by the isotropic Parrinello-Rahman barostat to control the pressure.[58] A cut-off of 1.0 nm is used for both the van der Waals and short-range Coulombic interactions. The long-range electrostatic interactions were calculated using the Particle Mesh Ewald (PME) method with a grid spacing of 0.16 and order of 4. The production NPT simulation of each system was run for 500 ns, and a time step of 2 fs was used. In the production simulations, all covalent bonds containing hydrogen atom were constrained using the LINCS algorithm.[59] GROMACS[50] version 2021.4.6 was used for all simulations. The VMD[60] software was used for the visualization of simulation trajectories and the preparation of figures. The GROMACS tools were used to perform the H-bond analysis, while the PLUMED[61] version 2.8.0 was used to perform the ligand reordering and coordination number analyses. The π-stack calculations and all the analyses graphs were generated using a few in-house Python codes.

OPES$_E$ simulation details

The dimerization simulations of MPCs were performed using the OPES$_E$ method implemented in PLUMED 2.8.0.[61] The OPES$_E$ simulations were performed using two CVs - s_1 (CV1): the COM-COM distance between the Au atoms of both MPCs and s_2 (CV2): the average solvent coordination within 1 nm distance cutoff of COM of MPC. In all the OPES$_E$ simulations, a barrier height (energy regulator) of 100 kJ/mol and adaptive sigma values were used. All OPES$_E$ simulations were carried out for $\sim$2 μs to have multiple barrier recrossing events and calculate the converged free energy profiles. The free energy profiles of

dimerization were calculated using a reweighing algorithm.[47]

Corresponding Author*

E-mail: tkarmakar@chemistry.iitd.ac.in

ORCID:

Tarak Karmakar: 0000-0002-8721-6247

Vikas Tiwari: 0000-0003-4510-253X

Present Address

Department of Chemistry

Indian Institute of Technology, Delhi

Hauz Khas, New Delhi 110016, India

Notes:

The authors declare no competing financial interest.

7. ACKNOWLEDGEMENTS

VT thanks PMRF for Ph. D. fellowship. TK acknowledges the Science and Engineering Research Board (SERB), New Delhi, India for the Start-up Research Grant (File No. SRG/2022/000969). We also acknowledge IIT Delhi for the Seed Grant. We thank IIT Delhi HPC facility for computational resources.

References

(1) Chakraborty, I.; Pradeep, T. Atomically Precise Clusters of Noble Metals: Emerging Link between Atoms and Nanoparticles. *Chemical Reviews* **2017**, *117*, 8208–8271.

(2) Jin, R.; Zeng, C.; Zhou, M.; Chen, Y. Atomically Precise Colloidal Metal Nanoclusters and Nanoparticles: Fundamentals and Opportunities. *Chemical Reviews* **2016**, *116*, 10346–10413.

(3) Malola, S.; Häkkinen, H. Prospects and challenges for computer simulations of monolayer-protected metal clusters. *Nature Communications* **2021**, *12*.

(4) Nag, A.; Pradeep, T. Assembling Atomically Precise Noble Metal Nanoclusters Using Supramolecular Interactions. *ACS Nanoscience Au* **2022**, *2*, 160–178.

(5) Howes, P. D.; Chandrawati, R.; Stevens, M. M. Colloidal nanoparticles as advanced biological sensors. *Science* **2014**, *346*.

(6) Saha, K.; Agasti, S. S.; Kim, C.; Li, X.; Rotello, V. M. Gold Nanoparticles in Chemical and Biological Sensing. *Chemical Reviews* **2012**, *112*, 2739–2779.

(7) Sperling, R. A.; Gil, P. R.; Zhang, F.; Zanella, M.; Parak, W. J. Biological applications of gold nanoparticles. *Chemical Society Reviews* **2008**, *37*, 1896.

(8) Grönbeck, H. The bonding in thiolate protected gold nanoparticles from Au4f photoemission core level shifts. *Nanoscale* **2012**, *4*, 4178.

(9) Sun, C.; Mammen, N.; Kaappa, S.; Yuan, P.; Deng, G.; Zhao, C.; Yan, J.; Malola, S.; Honkala, K.; Häkkinen, H.; Teo, B. K.; Zheng, N. Atomically Precise, Thiolated Copper–Hydride Nanoclusters as Single-Site Hydrogenation Catalysts for Ketones in Mild Conditions. *ACS Nano* **2019**, *13*, 5975–5986.

(10) Longo, A.; Boed, E. J. J.; Mammen, N.; Linden, M.; Honkala, K.; Häkkinen, H.; Jongh, P. E.; Donoeva, B. Towards Atomically Precise Supported Catalysts from Monolayer-Protected Clusters: The Critical Role of the Support. *Chemistry – A European Journal* **2020**, *26*, 7051–7058.

(11) Mammen, N.; Malola, S.; Honkala, K.; Häkkinen, H. Selective Acrolein Hydrogenation over Ligand-Protected Gold Clusters: A Venus Flytrap Mechanism. *ACS Catalysis* **2022**, *12*, 2365–2374.

(12) Zhang, B.; Sels, A.; Salassa, G.; Pollitt, S.; Truttmann, V.; Rameshan, C.; Llorca, J.; Olszewski, W.; Rupprechter, G.; Bürgi, T.; Barrabés, N. Ligand Migration from Cluster to Support: A Crucial Factor for Catalysis by Thiolate-protected Gold Clusters. *ChemCatChem* **2018**, *10*, 5372–5376.

(13) Kang, X.; Chong, H.; Zhu, M. $Au_{25}(SR)_{18}$: the captain of the great nanocluster ship. *Nanoscale* **2018**, *10*, 10758–10834.

(14) Sudheeshkumar, V.; Sulaiman, K. O.; Scott, R. W. J. Activation of atom-precise clusters for catalysis. *Nanoscale Advances* **2020**, *2*, 55–69.

(15) Parker, J. F.; Fields-Zinna, C. A.; Murray, R. W. The Story of a Monodisperse Gold Nanoparticle: $Au_{25}(L)_{18}$. *Accounts of Chemical Research* **2010**, *43*, 1289–1296.

(16) Parker, J. F.; Weaver, J. E. F.; McCallum, F.; Fields-Zinna, C. A.; Murray, R. W. Synthesis of Monodisperse $[Oct_4N^+][Au_{25}(SR)_{18}{}^-]$ Nanoparticles, with Some Mechanistic Observations. *Langmuir* **2010**, *26*, 13650–13654.

(17) Zhu, M.; Lanni, E.; Garg, N.; Bier, M. E.; Jin, R. Kinetically Controlled, High-Yield Synthesis of $Au_{25}(SR)_{18}$ Clusters. *Journal of the American Chemical Society* **2008**, *130*, 1138–1139.

(18) Murray, R. W. Nanoelectrochemistry: Metal Nanoparticles, Nanoelectrodes, and Nanopores. *Chemical Reviews* **2008**, *108*, 2688–2720.

(19) Niihori, Y.; Hossain, S.; Sharma, S.; Kumar, B.; Kurashige, W.; Negishi, Y. Understanding and Practical Use of Ligand and Metal Exchange Reactions in Thiolate-Protected Metal Clusters to Synthesize Controlled Metal Clusters. *The Chemical Record* **2017**, *17*, 473–484.

(20) Chen, T.; Fung, V.; Yao, Q.; Luo, Z.; en Jiang, D.; Xie, J. Synthesis of Water-Soluble $[Au_{25}(SR)_{18}]^-$ Using a Stoichiometric Amount of $NaBH_4$. *Journal of the American Chemical Society* **2018**, *140*, 11370–11377.

(21) Shivhare, A.; Wang, L.; Scott, R. W. J. Isolation of Carboxylic Acid-Protected Au_{25} Clusters Using a Borohydride Purification Strategy. *Langmuir* **2015**, *31*, 1835–1841.

(22) Yu, Y.; Luo, Z.; Yu, Y.; Lee, J. Y.; Xie, J. Observation of Cluster Size Growth in CO-Directed Synthesis of $Au_{25}(SR)_{18}$ Nanoclusters. *ACS Nano* **2012**, *6*, 7920–7927.

(23) Kumar, S.; Jin, R. Water-soluble $Au_{25}(Capt)_{18}$ nanoclusters: synthesis, thermal stability, and optical properties. *Nanoscale* **2012**, *4*, 4222.

(24) Xu, Q.; Kumar, S.; Jin, S.; Qian, H.; Zhu, M.; Jin, R. Chiral 38-Gold-Atom Nanoclusters: Synthesis and Chiroptical Properties. *Small* **2013**, *10*, 1008–1014.

(25) Negishi, Y.; Takasugi, Y.; Sato, S.; Yao, H.; Kimura, K.; Tsukuda, T. Magic-Numbered Au_n Clusters Protected by Glutathione Monolayers (n = 18, 21, 25, 28, 32, 39): Isolation and Spectroscopic Characterization. *Journal of the American Chemical Society* **2004**, *126*, 6518–6519.

(26) Negishi, Y.; Nobusada, K.; Tsukuda, T. Glutathione-Protected Gold Clusters Revisited: Bridging the Gap between Gold(I)-Thiolate Complexes and Thiolate-Protected Gold Nanocrystals. *Journal of the American Chemical Society* **2005**, *127*, 5261–5270.

(27) Li, Y.; Zhai, T.; Chen, J.; Shi, J.; Wang, L.; Shen, J.; Liu, X. Water-Dispersible Gold Nanoclusters: Synthesis Strategies, Optical Properties, and Biological Applications. *Chemistry – A European Journal* **2021**, *28*.

(28) Tao, Y.; Li, M.; Ren, J.; Qu, X. Metal nanoclusters: novel probes for diagnostic and therapeutic applications. *Chemical Society Reviews* **2015**, *44*, 8636–8663.

(29) Shang, L.; Dong, S.; Nienhaus, G. U. Ultra-small fluorescent metal nanoclusters: Synthesis and biological applications. *Nano Today* **2011**, *6*, 401–418.

(30) Bhattacharya, S. R.; Bhattacharya, K.; Xavier, V. J.; Ziarati, A.; Picard, D.; Bürgi, T. The Atomically Precise Gold/Captopril Nanocluster $Au_{25}(SR)_{18}$ Gains Anticancer Activity by Inhibiting Mitochondrial Oxidative Phosphorylation. *ACS Applied Materials & Interfaces* **2022**, *14*, 29521–29536.

(31) Tavanti, F.; Pedone, A.; Menziani, M. C.; Alexander-Katz, A. Computational Insights into the Binding of Monolayer-Capped Gold Nanoparticles onto Amyloid- Fibrils. *ACS Chemical Neuroscience* **2020**, *11*, 3153–3160.

(32) Qi, J.; Liu, Y.; Xu, H.; Xue, T.; Su, Y.; Lin, Z. Anti-cancer effect of melittin-Au25(MHA)18 complexes on human cervical cancer HeLa cells. *Journal of Drug Delivery Science and Technology* **2022**, *68*, 103078.

(33) Tiwari, V.; Garg, S.; Karmakar, T. Insights into the Interactions of Peptides with Monolayer-Protected Metal Nanoclusters. *ACS Applied Bio Materials* **2023**,

(34) Dutta, S.; Corni, S.; Brancolini, G. Molecular Dynamics Simulations of a Catalytic Multivalent Peptide–Nanoparticle Complex. *International Journal of Molecular Sciences* **2021**, *22*, 3624.

(35) Brancolini, G.; Tozzini, V. Multiscale modeling of proteins interaction with functionalized nanoparticles. *Current Opinion in Colloid & Interface Science* **2019**, *41*, 66–73.

(36) Lin, Y.; Charchar, P.; Christofferson, A. J.; Thomas, M. R.; Todorova, N.; Mazo, M. M.; Chen, Q.; Doutch, J.; Richardson, R.; Yarovsky, I.; Stevens, M. M. Surface Dynamics and Ligand–Core Interactions of Quantum Sized Photoluminescent Gold Nanoclusters. *Journal of the American Chemical Society* **2018**, *140*, 18217–18226.

(37) Shen, Z.; Baker, W.; Ye, H.; Li, Y. pH-Dependent aggregation and pH-independent cell membrane adhesion of monolayer-protected mixed charged gold nanoparticles. *Nanoscale* **2019**, *11*, 7371–7385.

(38) Vanzan, M.; Rosa, M.; Corni, S. Atomistic insight into the aggregation of $[Au_{25}(SR)_{18}$ nanoclusters. *Nanoscale Advances* **2020**, *2*, 2842–2852.

(39) Yuan, P.; Zhang, R.; Selenius, E.; Ruan, P.; Yao, Y.; Zhou, Y.; Malola, S.; Häkkinen, H.; Teo, B. K.; Cao, Y.; Zheng, N. Solvent-mediated assembly of atom-precise gold–silver nanoclusters to semiconducting one-dimensional materials. *Nature Communications* **2020**, *11*.

(40) Nonappa,; Lahtinen, T.; Haataja, J. S.; Tero, T.-R.; Häkkinen, H.; Ikkala, O. Template-Free Supracolloidal Self-Assembly of Atomically Precise Gold Nanoclusters: From 2D Colloidal Crystals to Spherical Capsids. *Angewandte Chemie International Edition* **2016**, *55*, 16035–16038.

(41) Salorinne, K.; Malola, S.; Wong, O. A.; Rithner, C. D.; Chen, X.; Ackerson, C. J.; Häkkinen, H. Conformation and dynamics of the ligand shell of a water-soluble Au102 nanoparticle. *Nature Communications* **2016**, *7*.

(42) Goswami, N.; Zheng, K.; Xie, J. Bio-NCs – the marriage of ultrasmall metal nanoclusters with biomolecules. *Nanoscale* **2014**, *6*, 13328–13347.

(43) Koivisto, J.; Chen, X.; Donnini, S.; Lahtinen, T.; Häkkinen, H.; Groenhof, G.; Pettersson, M. Acid–Base Properties and Surface Charge Distribution of the Water-Soluble

Ausub102/sub(ip/iMBA)sub44/sub Nanocluster. *The Journal of Physical Chemistry C* **2016**, *120*, 10041–10050.

(44) Joshi, C. P.; Bootharaju, M. S.; Alhilaly, M. J.; Bakr, O. M. [Agsub25/sub(SR)sub18/sub]sup-/sup: The "Golden" Silver Nanoparticle. *Journal of the American Chemical Society* **2015**, *137*, 11578–11581.

(45) Lehn, R. C. V.; Atukorale, P. U.; Carney, R. P.; Yang, Y.-S.; Stellacci, F.; Irvine, D. J.; Alexander-Katz, A. Effect of Particle Diameter and Surface Composition on the Spontaneous Fusion of Monolayer-Protected Gold Nanoparticles with Lipid Bilayers. *Nano Letters* **2013**, *13*, 4060–4067.

(46) Correction: Membrane Partitioning of Anionic, Ligand-Coated Nanoparticles Is Accompanied by Ligand Snorkeling, Local Disordering, and Cholesterol Depletion. *PLOS Computational Biology* **2016**, *12*, e1004769.

(47) Invernizzi, M.; Parrinello, M. Rethinking Metadynamics: From Bias Potentials to Probability Distributions. *The Journal of Physical Chemistry Letters* **2020**, *11*, 2731–2736.

(48) Invernizzi, M.; Parrinello, M. Exploration vs Convergence Speed in Adaptive-Bias Enhanced Sampling. *Journal of Chemical Theory and Computation* **2022**, *18*, 3988–3996.

(49) Yao, Q.; Liu, L.; Malola, S.; Ge, M.; Xu, H.; Wu, Z.; Chen, T.; Cao, Y.; Matus, M. F.; Pihlajamäki, A.; Han, Y.; Häkkinen, H.; Xie, J. Supercrystal engineering of atomically precise gold nanoparticles promoted by surface dynamics. *Nature Chemistry* **2022**, *15*, 230–239.

(50) Berendsen, H.; van der Spoel, D.; van Drunen, R. GROMACS: A message-passing parallel molecular dynamics implementation. *Computer Physics Communications* **1995**, *91*, 43–56.

(51) Hanwell, M. D.; Curtis, D. E.; Lonie, D. C.; Vandermeersch, T.; Zurek, E.; Hutchison, G. R. Avogadro: an advanced semantic chemical editor, visualization, and analysis platform. *Journal of Cheminformatics* **2012**, *4*.

(52) Franco-Ulloa, S.; Riccardi, L.; Rimembrana, F.; Pini, M.; Vivo, M. D. NanoModeler: A Webserver for Molecular Simulations and Engineering of Nanoparticles. *Journal of Chemical Theory and Computation* **2019**, *15*, 2022–2032.

(53) Franco-Ulloa, S.; Riccardi, L.; Rimembrana, F.; Grottin, E.; Pini, M.; Vivo, M. D. NanoModeler CG: A Tool for Modeling and Engineering Functional Nanoparticles at a Coarse-Grained Resolution. *Journal of Chemical Theory and Computation* **2023**, *19*, 1582–1591.

(54) Pohjolainen, E.; Chen, X.; Malola, S.; Groenhof, G.; Häkkinen, H. A Unified AMBER-Compatible Molecular Mechanics Force Field for Thiolate-Protected Gold Nanoclusters. *Journal of Chemical Theory and Computation* **2016**, *12*, 1342–1350.

(55) Heinz, H.; Vaia, R. A.; Farmer, B. L.; Naik, R. R. Accurate Simulation of Surfaces and Interfaces of Face-Centered Cubic Metals Using 12-6 and 9-6 Lennard-Jones Potentials. *The Journal of Physical Chemistry C* **2008**, *112*, 17281–17290.

(56) Wang, J.; Wolf, R. M.; Caldwell, J. W.; Kollman, P. A.; Case, D. A. Development and testing of a general amber force field. *Journal of Computational Chemistry* **2004**, *25*, 1157–1174.

(57) Berendsen, H. J. C.; Postma, J. P. M.; van Gunsteren, W. F.; DiNola, A.; Haak, J. R. Molecular dynamics with coupling to an external bath. *The Journal of Chemical Physics* **1984**, *81*, 3684–3690.

(58) Parrinello, M.; Rahman, A. Polymorphic transitions in single crystals: A new molecular dynamics method. *Journal of Applied Physics* **1981**, *52*, 7182–7190.

(59) Hess, B.; Bekker, H.; Berendsen, H. J. C.; Fraaije, J. G. E. M. LINCS: A linear constraint solver for molecular simulations. *Journal of Computational Chemistry* **1997**, *18*, 1463–1472.

(60) Humphrey, W.; Dalke, A.; Schulten, K. VMD: Visual molecular dynamics. *Journal of Molecular Graphics* **1996**, *14*, 33–38.

(61) Tribello, G. A.; Bonomi, M.; Branduardi, D.; Camilloni, C.; Bussi, G. PLUMED 2: New feathers for an old bird. *Computer Physics Communications* **2014**, *185*, 604–613.